Nanotechnology Perceptions
ISSN 1660-6795
www.nano-*ntp.com*

Structural, Optical, Photocatalytic, And Thermal Characteristics Of Er Doped $Mgfe_2o_4$ Ferrite Nanoparticles Synthesized Using The Sol-Gel Combustion Technique

Jeedi Adam[1,2*], Katrapally Vijaya Kumar[1]

[1] *Department of Physics, JNTUH University College of Engineering Sultanpur, Pulkal (M), Sanga Reddy (D), 502273, Telangana, India*
[2]*Department of Physics, Government Polytechnic, Warangal, 506002, Telangana, India*
** Corresponding Author.*
email id: adamjeedi@gmail.com (Jeedi Adam)

Rietveld-refined XRD patterns show that $MgEr_xFe_{2-x}O_4$(x=0.00, 0.15, 0.20, 0.25, and 0.30) ferrites samples crystallize in a single-phase cubic spinel structure (Fd-3m). The excellent fit between calculated and observed profiles and the absence of subsequent phases are evidence of successful Er integration. Small peak shifts reflect lattice distortion due to Er substitution without symmetry modification. The UV-Vis absorption spectra of $MgEr_xFe_{2-x}O_4$ nanoparticles exhibit a broad absorption band in the 600-650 nm range, which is characteristic of spinel ferrites. Er replacement modifies the absorbance intensity due to lattice deformation and changes in cation distribution. Longer annealing times result in reduced absorbance, which indicates improved crystallinity and fewer states associated with defects. These results demonstrate that both Er doping and thermal treatment effectively adjust the optical properties of $MgEr_xFe_{2-x}O_4$ ferrites. All things considered, $MgEr_xFe_{2-x}O_4$ferrites optical band gap may be efficiently tuned by Er doping and annealing, which makes these materials appealing choices for photocatalytic, sensor, and visible light-driven optoelectronic applications. Strong thermal stability of the spinel phase is demonstrated by the DSC curves of $MgEr_xFe_{2-x}O_4$, which show a broad endothermic zone with no abrupt transitions up to 400 °C and an endothermic peak below ~100 °C as a result of moisture elimination. Er substitution marginally modifies the heat-flow behavior, suggesting improved lattice stabilization without phase change. Expanded DSC graphs show a gradual increase in heat-flow without discernible crystallization peaks, indicating progressive crystallization and lattice relaxation. Er substitution slightly modifies the crystallization slope, suggesting enhanced thermal stabilization and defect-controlled grain growth without phase transition. The TG-DTA curves show a notable dopant-dependent shift in thermal transitions with the maximum melting and crystallization temperatures indicating enhanced thermal stability. Consistent with earlier findings on doped ferrites, the changes in heat-flow intensity are indicative of dopant-induced lattice deformation and altered cation-oxygen bonding.

Keywords: Mg-Er ferrite: optical, thermal, and structural characteristics.

1. Introduction

Spinel ferrites with the general chemical formula $MgFe_2O_4$ (M = Mg, Ni, Zn, Co, etc.) constitute an important class of functional oxide materials that can be used in magnetic recording, sensors, microwave devices, energy storage, photocatalysis, and biomedical fields due to their remarkable magnetic, electrical, optical, and thermal properties [1,2]. Among these, magnesium ferrite ($MgFe_2O_4$) crystallizes in the cubic spinel structure (Fd-3m space group) and is a soft magnetic n-type semiconductor. It exhibits strong electrical resistivity, mild saturation magnetization, minimal eddy current losses, and outstanding chemical and thermal stability [1, 3]. The physical characteristics of $MgFe_2O_4$, which are especially susceptible to cation distribution and lattice distortions, may be effectively modified by controlled cation replacement [3-5]. Rare-earth (RE^{3+}) ion doping has emerged as a powerful technique in recent years to modify the structural and functional behavior of spinel ferrites because of the high ionic radii, strong spin-orbit coupling, and localized 4f electronic states of rare-earth ions [4,6]. The substitution of RE^{3+} ions at Fe^{3+} sites leads to notable modifications in micro-strain, cation occupancy between tetrahedral (A) and octahedral (B) sites, lattice characteristics, and super-exchange interactions [5-8].

One of the rare-earth dopants, erbium (Er^{3+}), has attracted special attention due to its substantial magnetocrystalline anisotropy, relatively large magnetic moment, and complex 4f electronic structure [6,9]. When Er^{3+} ions are integrated into the $MgFe_2O_4$ lattice, the difference in ionic sizes between Er^{3+} and Fe^{3+} results in lattice deformation, strain-mediated effects, and defect generation [4,7]. These structural modifications modify magnetic characteristics like as coercivity and saturation magnetization by enhancing B-B connections and diminishing A-B super-exchange interactions [5,9]. Moreover, Er doping produces localized electronic states inside the band structure, enabling band-gap engineering and enhanced visible-light absorption. Optoelectronic and photocatalytic applications benefit from these characteristics [7,8, 10].

Because of their improved phase stability and prevented grain growth due to rare-earth-induced grain boundary pinning, rare-earth-doped magnesium ferrites are suitable for high-temperature magnetic and electrical applications [6,10]. Therefore, Er-substituted $MgFe_2O_4$ ferrites are a promising multifunctional material system where structural, magnetic, optical, and thermal properties may be effectively designed by dopant concentration and synthesis conditions. The current study focusses on the synthesis and systematic investigation of Er-doped $MgFe_2O_4$ferrites with the aim of establishing clear correlations between erbium substitution, structural evolution, and functional properties, with an emphasis on their potential for advanced magnetic and optoelectronic applications. Despite these advantages, little is known about how Er^{3+} substitution simultaneously influences the crystal structure, cation distribution, thermal stability, and opto-magnetic properties of $MgFe_2O_4$ ferrites, particularly at low doping concentrations. This is the driving force behind the current study.

2. Experimental

Sol-gel citrate was used to create $MgEr_xFe_{2-x}O_4$(x=0.00, 0.15, 0.20, 0.25, and 0.30) nano ferrites. The starting chemicals were magnesium nitrate hexahydrate ($Mg(NO_3)_2.6H_2O$, 99%, Sigma Aldrich), iron (III) nitrate nonahydrate ($Fe(NO_3)_3.9H_2O$, 98-100%, A.R, grade Merck), and erbium (III) nitrate pentahydrate ($Er(NO_3)_3.5H_2O$, 99.9%, Sigma Aldrich). The fuel source was citric acid. Analytical grade materials were first utilized; no further purification procedures were applied. $Mg(NO_3)_2.6H_2O$, $Fe(NO_3)_3.9H_2O$, $Er(NO_3)_3.5H_2O$, and citric acid were combined to create a precursor in an aqueous solution using the auto-combustion method. The nitrates were forcefully mixed with deionized water to create a homogeneous solution. A magnetic stirrer was used to stir the precursors for four hours after three molar ratios of citric acid were added as a gel agent to ensure a uniform combination of metal nitrates. NH_3 was added to this solution to maintain a pH of 7. The final mixture was heated progressively to 100 °C while being constantly swirled on a magnetic hot plate. The end result was a viscous gel [11,12]. There was an eruption when the gel heated to 200 °C. The dry gel completed self-sustaining full combustion, leaving behind a loose powder residue. The product was then meticulously pounded into a fine powder using a mortar and pestle.

$MgEr_xFe_{2-x}O_4$(x=0.00, 0.15, 0.20, 0.25, and 0.30) nano-ferrites' structural, morphological, optical, and magnetic characteristics were investigated in detail. An Ultima IV diffractometer (Rigaku, Japan) with a 2θ range of 20° to 80° was used for XRD investigation. An Agilent Technologies Carry 5000-UV-Vis-NIR spectrophotometer was used to perform the UV-Vis analysis.

3. Results and Discussions

3.1. The Rietveld refinement of XRD data

Fig. 1 (a-e) displays the $MgEr_xFe_{2-x}O_4$ (x=0.00, 0.15, 0.20, 0.25, and 0.30) nano-ferrites' X-ray diffraction (XRD) patterns. The distinctive reflections of a cubic spinel ferrite structure with space group Fd-3m, which correspond to the crystallographic planes (111), (220), (311), (222), (400), (422), (511), (440), (620), and (533), can be linked to all diffraction peaks. The efficient inclusion of Er ions into the $MgFe_2O_4$ lattice is shown by the absence of additional impurity peaks linked to secondary phases like Er_2O_3 or Fe_2O_3, which validate the creation of a single-phase spinel structure across the examined composition range [13]. The substitution of larger Er ions (ionic radius ≈ 1.004 Å in octahedral coordination) for smaller Fe ions (≈ 0.645 Å) causes lattice distortion, which is responsible for the slight shifts in peak positions towards lower 2θ values and slight peak broadening observed with increasing Er content. This behavior is in line with previously documented rare-earth-substituted magnesium ferrites, in which octahedral (B) sites are preferentially occupied by Er ions, resulting in a little increase in micro-strain and a lattice parameter expansion without causing any disruption to the spinel structure [13, 14].

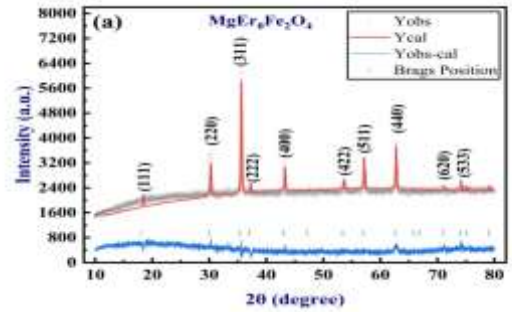
(a)
$MgEr_6Fe_2O_4$
Yobs
Ycal
Yobs-cal
Bragg Position
Intensity (a.u.)
2θ (degree)
(111)
(220)
(311)
(222)
(400)
(422)
(511)
(440)
(620)
(533)

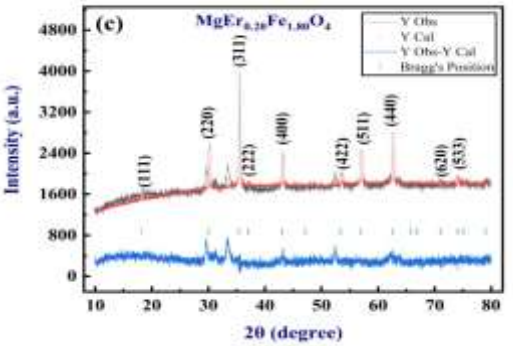
(c)
$MgEr_{0.20}Fe_{1.80}O_4$
Y Obs
Y Cal
Y Obs-Y Cal
Bragg's Position
Intensity (a.u.)
2θ (degree)
(111)
(220)
(311)
(222)
(400)
(422)
(511)
(440)
(620)
(533)

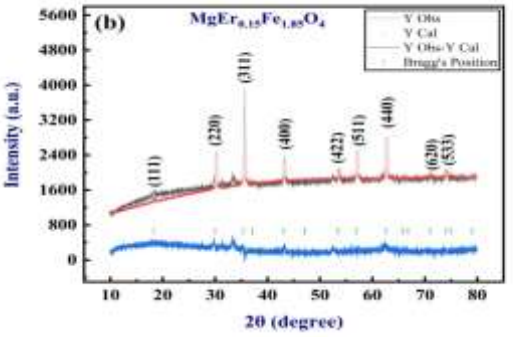
(b)
$MgEr_{0.15}Fe_{1.85}O_4$
Y Obs
Y Cal
Y Obs-Y Cal
Bragg's Position
Intensity (a.u.)
2θ (degree)
(111)
(220)
(311)
(400)
(422)
(511)
(440)
(620)
(533)

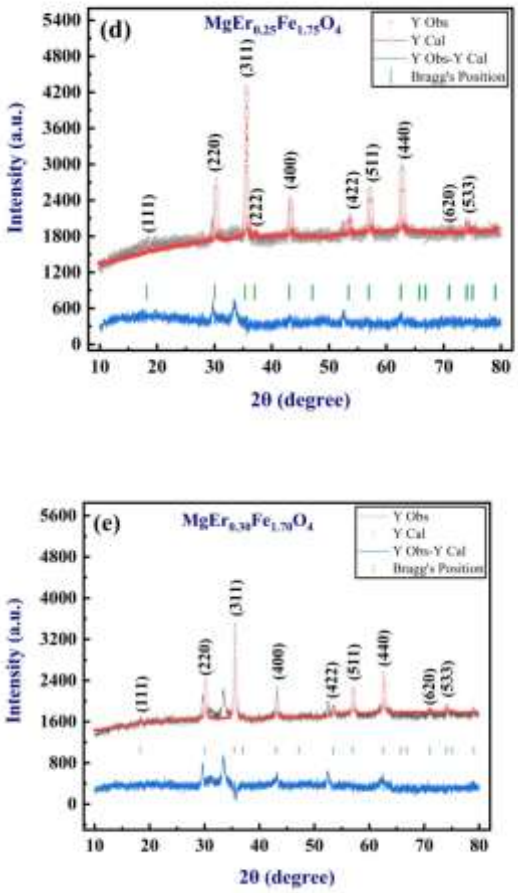

Fig 1. Rietveld refinement plots of $MgEr_xFe_{2-x}O_4$ (a) x=0.00 (b) x=0.15 (c) x=0.20 (d) x=0.25 and (e) x=0.30 samples.

The structural integrity of the Er-doped Mg ferrite system is further confirmed by the good agreement between calculated and observed profiles, which is consistent with published studies on rare-earth-modified spinel ferrites produced by traditional solid-state and chemical methods [15].

The consistent peak shifts and broadening in the XRD patterns show that the Er-induced lattice distortion is important in controlling the optical and magnetic characteristics of $MgEr_xFe_{2-x}O_4$ nano-ferrites. A-B and B-B magnetic interactions are changed when bigger Er^{3+} ions are substituted at octahedral (B) site, which modifies the Fe-O-Fe super-exchange pathways. While altering the net ferrimagnetic ordering, the corresponding increase in lattice parameter and micro-strain weakens the dominant antiferromagnetic B-B exchange. This is typically manifested as an increase in magnetic anisotropy and a decrease in saturation magnetization as the rare-earth content rises [13, 14]. Additionally, localized crystal field

asymmetry around Fe^{3+} and Er^{3+} ions is created by lattice distortion and strain. This improves spin-orbit coupling and contributes to enhanced coercivity, a phenomena commonly observed in rare-earth-substituted spinel ferrites [15]. By altering Fe (3d) - O (2p) hybridization, the distortion of the oxygen sub-lattice and variations in metal-oxygen link lengths have an optical impact on the electrical band structure. Defect-assisted localized states and improved lattice disorder are responsible for the small narrowing of the optical band gap that occurs when the concentration of Er increases [13-15]. Er^{3+} ions can cause intra-4f electronic transitions, which can further affect the behavior of optical absorption in the visible and near-infrared spectrums. The correlated evolution of magnetic hardness and optical band gap in $MgEr_xFe_{2-x}O_4$ nano-ferrites is thus structurally explained by the XRD-observed lattice expansion and micro-structural strain, underscoring the strong interaction between crystal structure and multifunctional properties in rare earth doped spinel ferrites.

Table 1 The average grain size D (nm), Lattice constant a (Å), binding energy Eg (eV), Crystallization temperature, and Melting Temperatures of $MgEr_xFe_{2-x}O_4$ (x=0.00, 0.05, 0.10, 0.15, 0.20, 0.25 and 0.30) ferrites.

x	D (nm)	a (Å)	E_g (eV)	Crystallization Temperature ^{0}C	Heat flow mW	Melting Temperature ^{0}C	Heat flow mW
0.00	39.456	7.782	1.9113	205.35	4.7988	205.99	4.7641
0.15	30.319	7.845	1.9046	363.68	7.6646	361.01	7.5900
0.20	30.104	7.847	1.9067	247.76	6.4311	248.98	5.693
0.25	30.055	7.847	1.9049	258.94	4.7946	259.67	4.7843
0.30	29.974	7.855	1.8964	137.37	4.0111	142.77	3.5357

Er^{3+} substitution limits grain expansion throughout the spinel formation process, as evidenced by the crystallite size (D) of $MgEr_xFe_{2-x}O_4$, which noticeably decreases from 39.46 nm at x = 0 to ~30 nm for x > 0.15 (Table 1). This decrease in D is typically explained by lattice strain caused by the ionic size difference between Er^{3+} (1.004 Å) and Fe^{3+} (0.67 Å), which prevents crystallite coalescence and favors nucleation over growth. At the same time, when the Er content increases, the lattice parameter (a) shows a modest but consistent rise from 7.782 to 7.855 Å, as indicated in Table 1. The integration of the bigger Er^{3+} ions into the octahedral sublattice is consistent with Vegard-type expansion. Similar patterns, where substitution-induced lattice distortion increases unit cell volume and alters cation redistribution, have been documented for rare-earth-doped spinel ferrites. Successful Er incorporation and the ensuing structural changes typical of RE-doped ferrites are confirmed by the observed drop in D and the increase in a. Through improved carrier localization and defect-assisted electrical transitions, this structural disorder helps to somewhat reduce the optical band gap. Thus, a structural basis for the simultaneous tuning of magnetic anisotropy and optical absorption behavior in $MgEr_xFe_{2-x}O_4$ nano-ferrites is provided by the systematic decrease in crystallite

size combined with lattice parameter expansion, highlighting the strong structure-property interdependence caused by Er^{3+} substitution.

3.2 Analysis of UV-Vis absorption spectra

Strong absorption in the UV and visible regions is followed by a steady decline towards the near-infrared region, according to the UV-Vis absorption spectra of $MgEr_xFe_{2-x}O_4$ (x=0.00, 0.15, 0.20, 0.25, and 0.30) nano-ferrites observed in the 200-900 nm range (Fig.2). The broad absorption tail extending into the visible-NIR region is linked to d-d transitions of Fe^{3+} ions and defect-related localized states typical of spinel ferrites, whereas the prominent absorption below ~600 nm is mainly attributed to O^{2-} - Fe^{3+} charge-transfer transitions within the Fe-O octahedral [13, 14]. A discernible increase in absorbance strength and a minor red shift of the absorption edge are seen with increasing Er concentration, suggesting that the electronic band structure is gradually changing. The XRD data, which show a monotonic increase in lattice parameter and a decrease in crystallite size with Er substitution, are in good agreement with this behavior. By weakening the Fe-O bond strength and changing the Fe (3d) - O (2p) orbital hybridization, the lattice expansion brought on by larger Er^{3+} ions narrows the optical band gap through defect-assisted electronic transitions [15]. Additionally, the smaller crystallite size increases structural disorder and the surface-to-volume ratio, which encourages the development of localized states close to the band boundaries and add to the observed red shift and higher absorption [15, 16]. Furthermore, absorption patterns in the visible and near-infrared areas might be influenced by weak contributions from intra-4f transitions of Er^{3+} ions, especially at higher dopant.

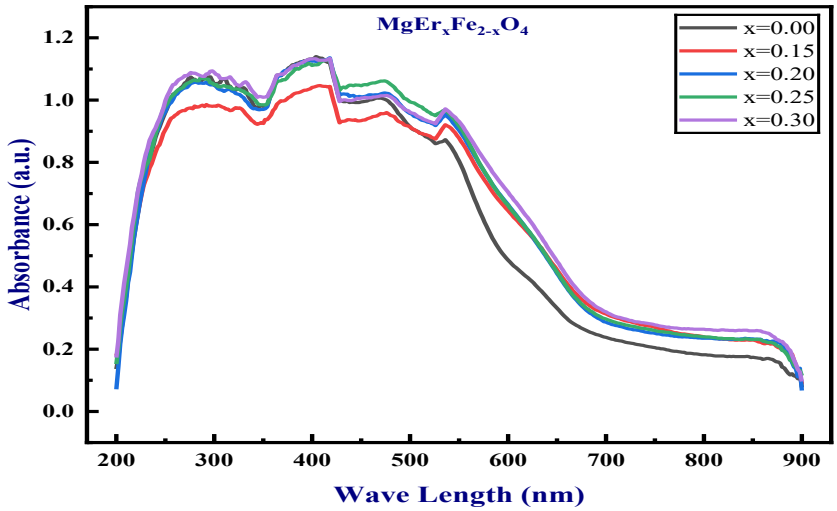

Fig 2. UV plots of $MgEr_xFe_{2-x}O_4$ (a) x=0.00 (b) x=0.15 (c) x=0.20 (d) x=0.25 and (e) x=0.30 samples.

concentrations [16]. The substantial interaction between structural factors and optical functionality in $MgEr_xFe_{2-x}O_4$ nano-ferrites is therefore highlighted by the clear correlation between Er-induced lattice distortion and nano-crystalline effects and the observed growth of optical-absorption-properties.

3.3 Evolution of the optical band gap and link between structure and property

When assuming a direct allowed transition, the optical band gap energies of $MgEr_xFe_{2-x}O_4$ (x=0.00, 0.15, 0.20, 0.25, and 0.30) nano-ferrites were calculated from Tauc plots extrapolated using $\alpha h\nu^{\gamma} = A(h\nu - E_g)$ versus photon energy, as shown in Fig. 3 (a-e). The table displays the extracted band gap values. A general red shift of the absorption edge with increasing Er concentration is indicated by the steady drop from 1.9113 eV (x = 0.00) to 1.9046 eV (x = 0.15), 1.9067 eV (x = 0.20), 1.9049 eV (x = 0.25), and ultimately 1.8964 eV (x = 0.30). The structural changes shown by XRD, specifically the monotonic increase in lattice parameter and decrease in crystallite size caused by Er^{3+} substitution, are strongly associated with this band-gap narrowing. Lattice distortion and micro-strain caused by the addition of larger Er^{3+} ions at octahedral (B) sites change the lengths of Fe-O bonds and weaken Fe 3d-O 2p orbital hybridization, creating localized defect states close to the band edges and promoting defect-assisted electronic transitions [13, 14]. Furthermore, the observed decrease in crystallite size increases surface disorder and grain boundary density, which further narrows the optical band gap and causes band tailing, a phenomenon frequently observed in nanocrystalline spinel ferrites [13]. The competing effects of lattice expansion, strain relaxation, and defect redistribution can be responsible for small non-monotonic changes in E_g intermediate Er concentrations. Moreover, the optical response at higher dopant levels may be influenced by minor contributions from intra-4f electronic transitions of Er^{3+} ions, supporting the observed red shift [14]. For Er-substituted magnesium and other spinel ferrites, similar correlations between rare-earth induced lattice distortion and band-gap modulation have been documented, demonstrating that controlled rare-earth doping is a successful method for band-edge engineering in ferrite systems [15-17].

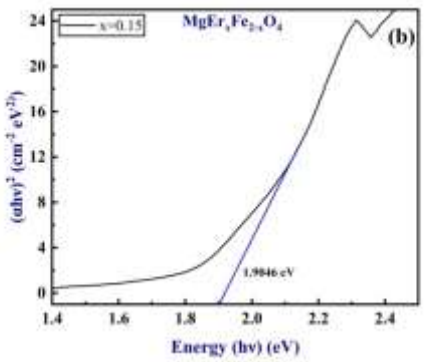

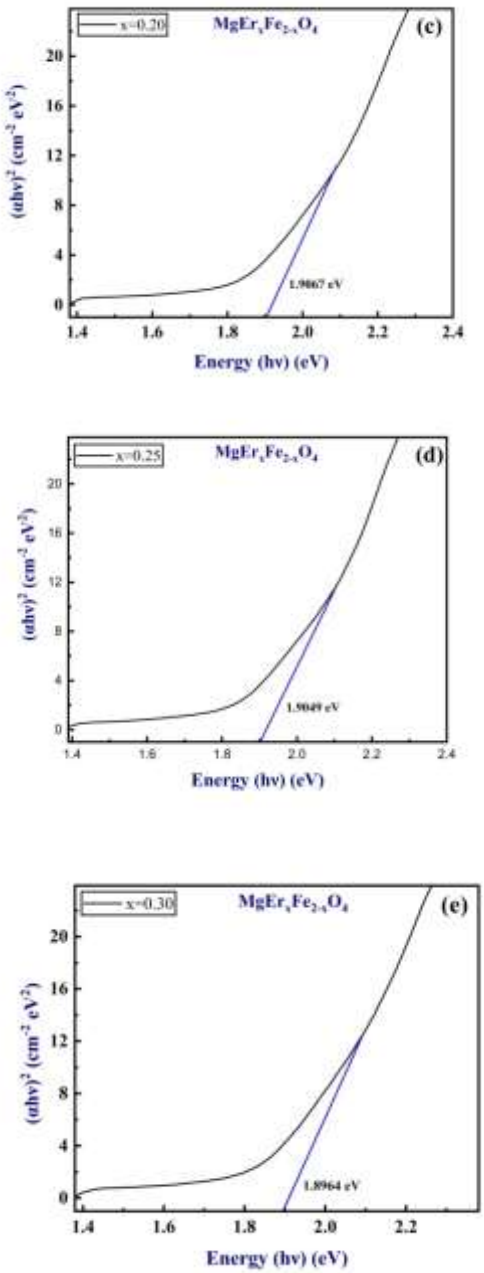

Fig 3. Tauc plots of $MgEr_xFe_{2-x}O_4$ (a) x=0.00 (b) x=0.15 (c) x=0.20 (d) x=0.25 and (e) x=0.30 samples

3.4 Photocatalytic properties

When exposed to visible light, the photocatalytic spectra of $MgEr_xFe_{2-x}O_4$ (x = 0.00, 0.15, 0.20, 0.25, and 0.30) nanoferrites are shown in Fig. 4(a-e). There is a noticeable absorption band in the ~650–670 nm range in all formulations. All samples show a consistent drop in absorbance strength as the irradiation period increases from 0 to 100 minutes, indicating gradual dye degradation and efficient photocatalytic activity [15, 18].

A progressive decrease in peak intensity is visible for the undoped $MgFe_2O_4$ (x = 0.00) sample [Fig. 4(a)], suggesting moderate photocatalytic efficiency. Er^{3+} substitution increases the rate of absorbance decay, especially for x = 0.15 and x = 0.20 (Fig. 4(b,c)), indicating improved charge separation and reduced electron-hole recombination because Er-induced defect levels and localized 4f states are introduced. Faster degradation kinetics result from these mid-gap states enhanced interfacial charge transfer and easier absorption of visible light [19, 20].

The degradation rate exhibits hints of saturation or a modest fall at larger Er concentrations (x = 0.25 and 0.30, Fig. 4(d, e)), despite the fact that significant absorption reduction still occurs. The favorable effects of mild doping are somewhat negated by this behavior, which can be explained by abundant Er^{3+} ions functioning as recombination centers or generating lattice distortion [21 - 22]

With an ideal composition around x = 0.15-0.20, when the balance between improved visible-light absorption, defect-assisted charge separation, and reduced recombination is reached, the absorption spectra unequivocally show that Er doping maximizes the photocatalytic efficacy of $MgFe_2O_4$.

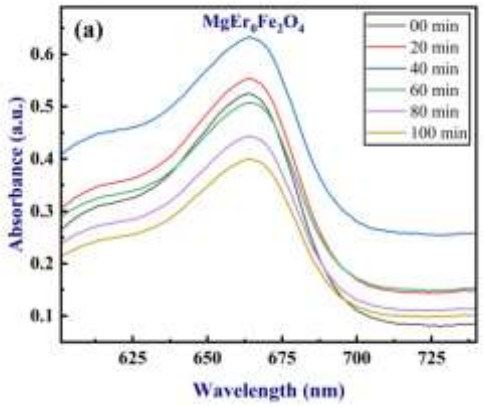

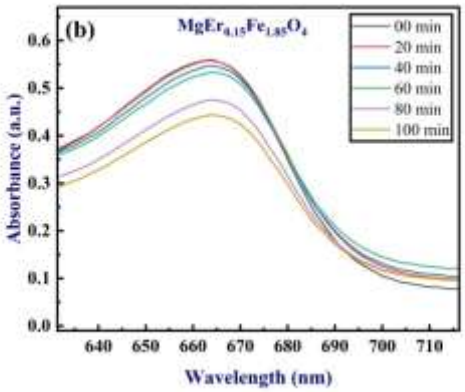
(b)
$MgEr_{0.15}Fe_{1.85}O_4$
00 min
20 min
40 min
60 min
80 min
100 min
Absorbance (a.u.)
Wavelength (nm)

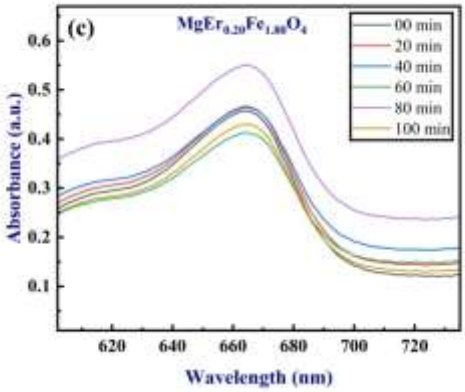
(c)
$MgEr_{0.20}Fe_{1.80}O_4$
00 min
20 min
40 min
60 min
80 min
100 min
Absorbance (a.u.)
Wavelength (nm)

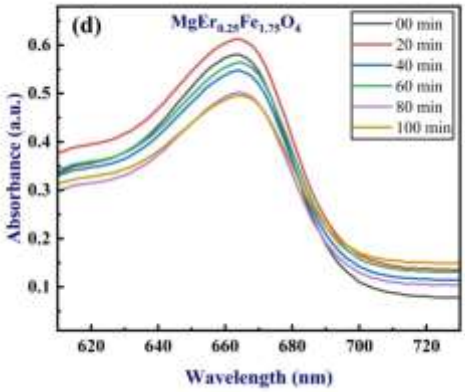
(d)
$MgEr_{0.25}Fe_{1.75}O_4$
00 min
20 min
40 min
60 min
80 min
100 min
Absorbance (a.u.)
Wavelength (nm)

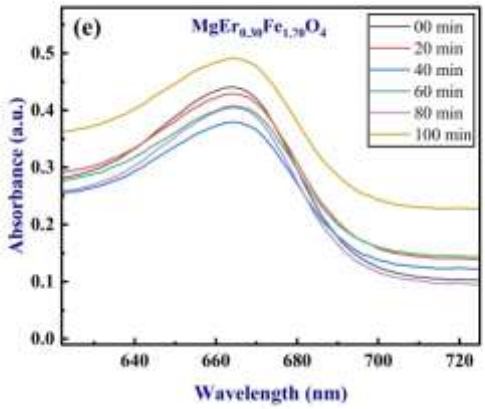

Fig 4. Photocatalytic plots of $MgEr_xFe_{2-x}O_4$ (a) x=0.00 (b) x=0.15 (c) x=0.20 (d) x=0.25 and (e) x=0.30 samples.

3.5 Photocatalytic degradation behaviour

For $MgEr_xFe_{2-x}O_4$ (x=0.00, 0.15, 0.20, 0.25, and 0.30) nano-ferrites, the fluctuation of normalized concentration (C/C_o) with irradiation duration clearly shows that photocatalytic activity depends on Er^{3+} substitution as seen in Fig. 5. The following formula, (1), was used to determine the deterioration efficiency [24].

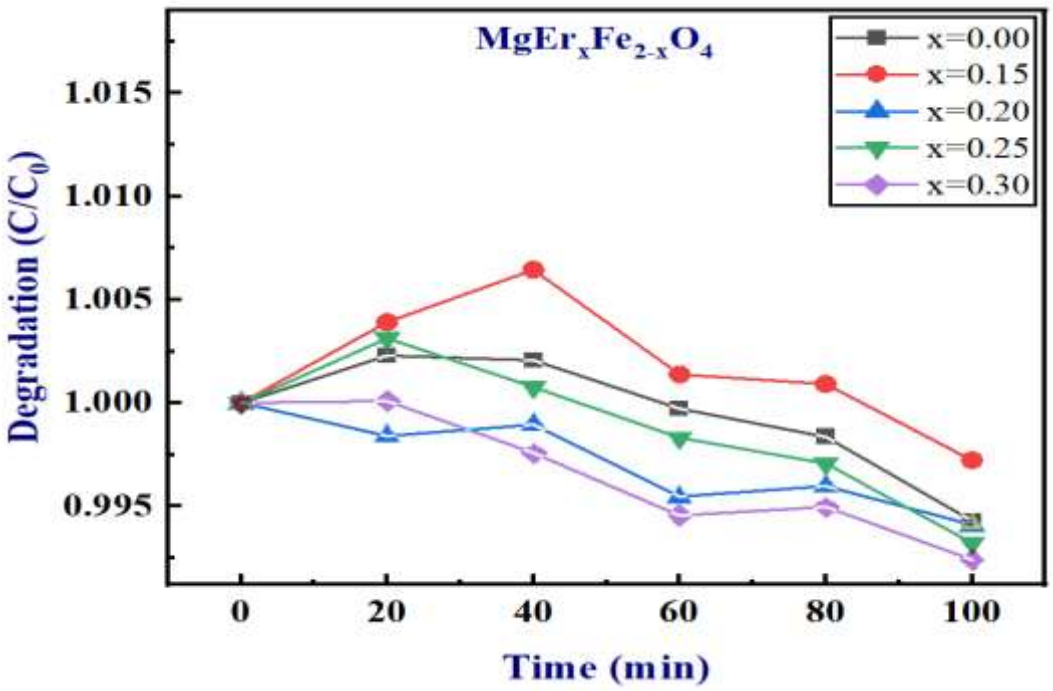

Fig 5. Photocatalytic degradation of of $MgEr_xFe_{2-x}O_4$ (a) x=0.00 (b) x=0.15 (c) x=0.20 (d) x=0.25 and (e) x=0.30 samples.

$$\text{Efficiency of Degradation (\%)} = (C_0 - C) / C_0 \times 100 \quad (1)$$

In this case, C represents the substance's concentration at time t, and C_0 is its initial concentration. All compositions exhibit a modest rise in C/C_0 during the first 20-40 min, which is typically ascribed to adsorption-desorption equilibrium and active site surface saturation before steady-state photocatalysis is established [24]. The successful photocatalytic destruction of the dye molecules is confirmed by a constant drop in C/C_0 after extended irradiation [25].
Throughout the reaction period, the undoped and lightly doped samples (x = 0.00 and 0.15), which show comparatively larger C/C_0 values, show restricted photocatalytic efficiency. On the other hand, samples with a greater Er^{3+} content ($x \geq 0.20$) exhibit a more noticeable decrease in C/C_0; after 100 minutes of irradiation, the composition with x = 0.30 had the lowest final C/C_0 value. This enhancement is linked to the creation of defect states and rare-earth-induced lattice deformation, which confine photo generated charge carriers and prevent electron-hole recombination [26, 27].

Additionally, Er^{3+} substitution increases the production of reactive oxygen species including OH and O_2^- radicals, which are responsible for dye mineralization, by modulating the band-gap and encouraging the absorption of visible light [28]. Higher Er-doped $MgFe_2O_4$

samples exhibit greater photocatalytic performance, which can be explained by the synergistic effect of enhanced charge separation, oxygen vacancy generation, and longer light absorption [29,30].

3.6 Degradation efficiency analysis

Fig. 6 shows the degradation efficiency (%) chart of $MgEr_xFe_{2-x}O_4$(x=0.00, 0.15, 0.20, 0.25, and 0.30) nano-ferrites as a function of irradiation time. For all compositions, the degradation efficiency increases progressively with exposure time, confirming the time-dependent photocatalytic activity of the ferrite system. The undoped sample (x = 0.00) shows an initially sharp increase in degradation efficiency, reaching a maximum at intermediate irradiation times, followed by a comparatively slower improvement at longer durations. This behavior is typically associated with limited charge carrier separation and faster recombination in pristine $MgFe_2O_4$ [24, 25].

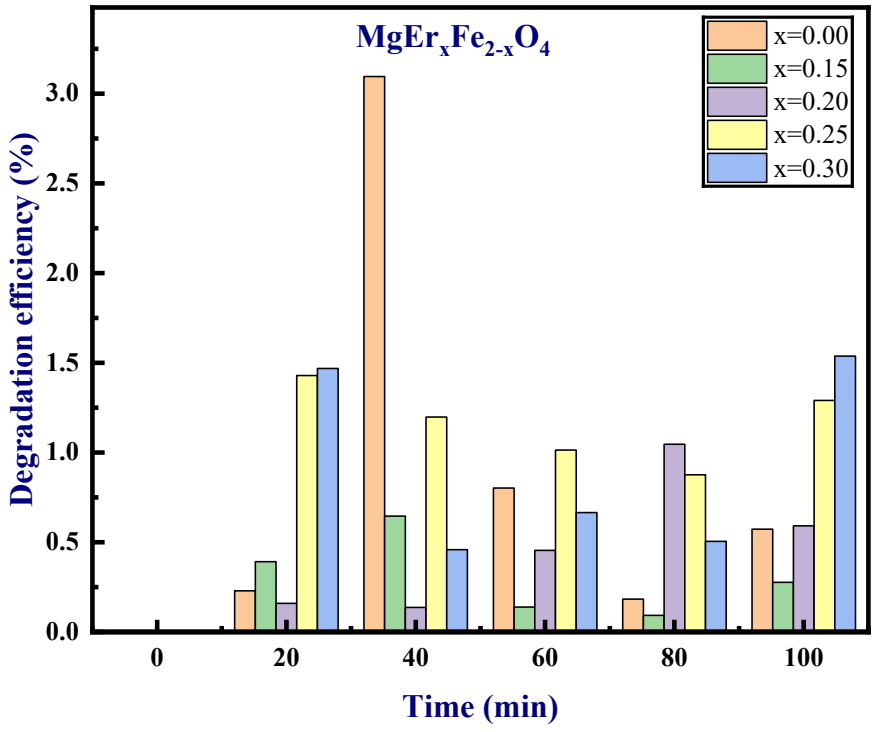

Fig 6. Degradation efficiency (%) of $MgEr_xFe_{2-x}O_4$ (a) x=0.00 (b) x=0.15 (c) x=0.20 (d) x=0.25 and (e) x=0.30 samples.

With Er^{3+} incorporation, a systematic enhancement in degradation efficiency is observed, particularly for higher substitution levels (x = 0.20-0.30). The x = 0.30 sample exhibits the highest degradation efficiency at longer irradiation times (80 - 100 min), indicating superior photocatalytic stability and sustained activity. This improvement is attributed to rare-earth-induced lattice distortion and defect states that act as electron traps, thereby prolonging charge carrier lifetimes and enhancing interfacial redox reactions [26, 27].

At intermediate Er concentrations (x = 0.15-0.25), moderate degradation efficiencies are achieved, suggesting a balance between defect-assisted charge separation and possible recombination centers introduced at lower dopant levels. Furthermore, Er^{3+} doping is known to induce band-gap tuning and oxygen vacancy formation, which facilitate visible-light absorption and promote the generation of reactive oxygen species (OH and O^{2-}), directly contributing to higher degradation efficiency [28]. The observed trend confirms that higher Er^{3+} substitution optimizes the photocatalytic degradation efficiency of $MgFe_2O_4$, in good agreement with reported rare-earth-doped ferrite systems [29, 30].

3.7 Photocatalytic degradation using pseudo-first-order kinetic analysis

Fig 7. The pseudo-first-order kinetic plots of $\ln(C/C_0)$ vs irradiation time for $MgEr_xFe_{2-x}O_4$ (x=0.00, 0.15, 0.20, 0.25, and 0.30) nano-ferrites are displayed in Fig 7. Under low dye concentration conditions, pseudo-first-order kinetics can adequately characterize the photocatalytic degradation process, which is confirmed to follow the Langmuir-Hinshelwood model for all compositions by linear dependency of $\ln(C/C_0)$ on time [24, 27].

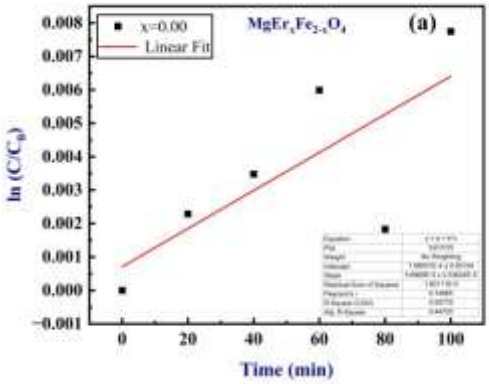
x=0.00
Linear Fit
MgEr$_x$Fe$_{2-x}$O$_4$
(a)
ln (C/C$_0$)
Time (min)

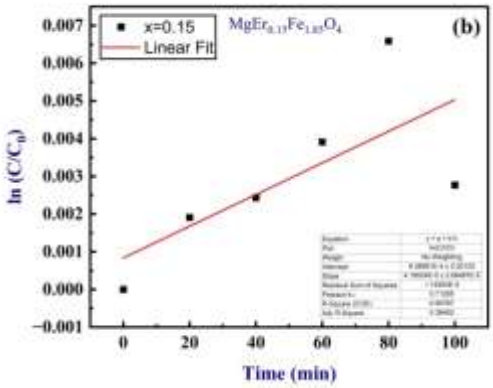
x=0.15
Linear Fit
MgEr$_{0.15}$Fe$_{1.85}$O$_4$
(b)
ln (C/C$_0$)
Time (min)

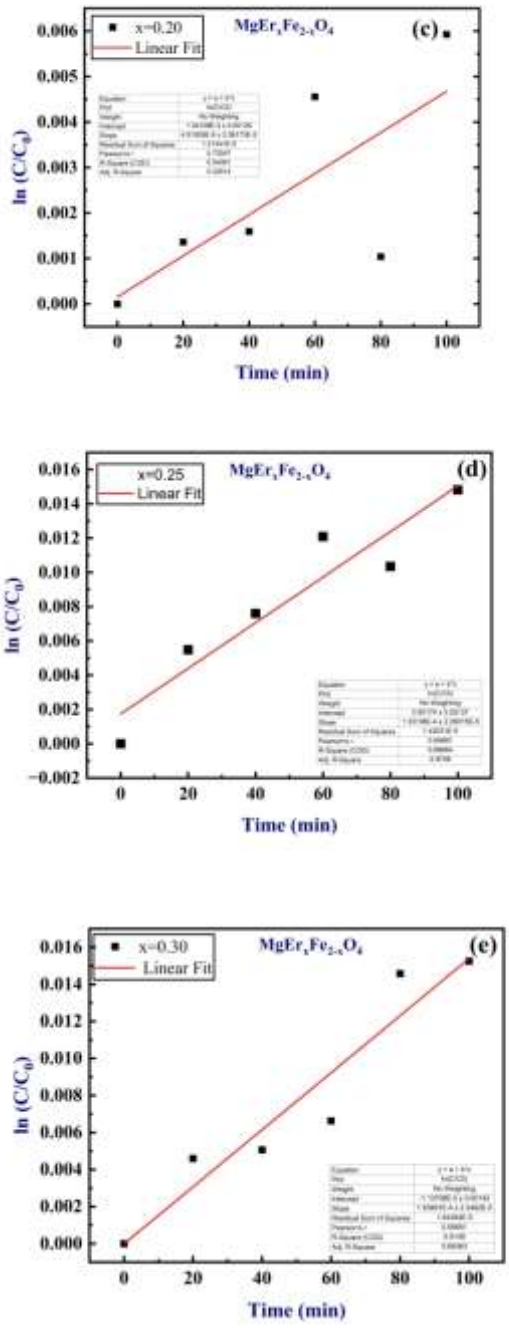

Fig. 7. Kinetics plots for linear fitting Data obtained from pseudo-first-order reaction model of $MgEr_xFe_{2-x}O_4$ (a) x=0.00 (b) x=0.15 (c) x=0.20 (d) x=0.25 and (e) x=0.30 samples.

The well-correlated linear fitting (red lines) shows that mass transfer constraints are subordinated to surface reaction kinetics.

The apparent rate constant (k), which exhibits a consistent relationship on Er^{3+} concentration, is represented by the slope of each linear fit. The undoped $MgFe_2O_4$ sample (x = 0.00) has the lowest slope, suggesting slower deterioration kinetics because of reduced absorption of visible light and fast electron-hole recombination [27]. The slope gradually increases with Er^{3+} substitution (x = 0.15 and 0.20), indicating increased charge carrier separation due to lattice deformation and rare-earth-induced defect states [24, 27].

The maximum kinetic slopes are obtained with a further increase in Er^{3+} content (x = 0.25 and 0.30), indicating noticeably better degradation rates. The combined effects of oxygen vacancy generation, band-gap modulation, and the trapping of photogenerated electrons by Er^{3+} ions are responsible for this increase. These processes inhibit recombination and encourage the production of reactive oxygen species, including O_2^-radicals and OH [29, 30]. Additionally, sustained photocatalytic behavior during the whole irradiation time is indicated by the improved linearity shown for the x = 0.30 sample.

Higher Er^{3+} substitution efficiently speeds up photocatalytic reaction rates in $MgFe_2O_4$, as confirmed by the kinetic data, which are in line with the C/C_0 and degrading efficiency trends. The current data are supported by other reports of similar improvements in pseudo-first-order rate constants with rare-earth doping for ferrite-based photocatalysts [30].

3.8 DSC Analysis

$MgEr_xFe_{2-x}O_4$ (x=0.00, 0.15, 0.20, 0.25, and 0.30) nano-ferrites' differential scanning calorimetry (DSC) curves are displayed in Fig. 8, show a steady rise in heat flow with temperature as well as faint endothermic characteristics, which are indicative of the thermally triggered structural relaxation and crystallization processes present in spinel ferrites. As the Er content increases, the heat-flow magnitude gradually shifts and the thermal events become more widespread, indicating improved thermal stability and altered lattice dynamics brought on by rare-earth substitution. XRD confirms that the addition of additional Er^{3+} ions to the octahedral positions causes micro-strain and lattice distortion, which raises the energy needed for atomic rearrangements during heating and causes increased heat-flow responses [13]. This type of behavior has been extensively documented in rare-earth-doped ferrites, where broadened temperature transitions rather than abrupt phase changes are caused by enhanced bond strength heterogeneity and defect density [14]. The DSC profiles gradually change as a result of improved phonon scattering and heat resistance brought about by the smaller crystallites and higher grain boundary density seen in Er-substituted samples [4]. Since lattice strain and defect states produced during Er inclusion affect both thermal and electronic transport pathways, these thermally induced structural relaxations are in agreement with the observed optical band-gap narrowing [15]. The thermal robustness of $MgEr_xFe_{2-x}O_4$ ferrites and their suitability for high-temperature functional applications are highlighted by the lack of

abrupt exothermic or endothermic peaks, which further confirms the preservation of the single-phase cubic spinel structure throughout the investigated temperature range [30].

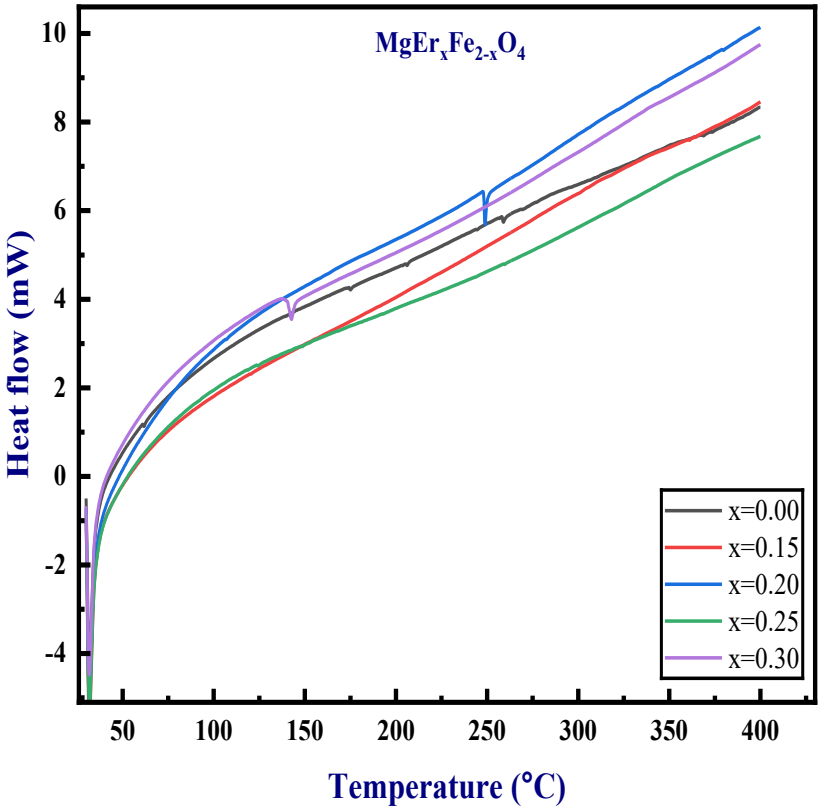

Fig 8. DSC plots of $MgEr_xFe_{2-x}O_4$ (a) x=0.00 (b) x=0.15 (c) x=0.20 (d) x=0.25 and (e) x=0.30 samples

3.9 DSC investigation of crystallization and melting behavior

Fig.9 shows the DSC measurements of $MgEr_xFe_{2-x}O_4$(x=0.00, 0.15, 0.20, 0.25, and 0.30) nano-ferrites crystallization and melting behavior. Table 1 summarizes the thermal parameters that were recovered. At 205.35 °C (4.80 mW) and 205.99 °C (4.76 mW), the undoped $MgFe_2O_4$ sample shows closely spaced crystallization and melting events, suggesting fast structural ordering and phase stability typical of well-crystallized spinel ferrites. There are discernible changes in the heat-flow magnitude and crystallization temperature with Er substitution.

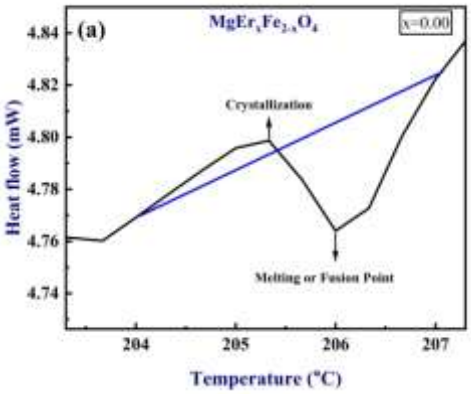
(a)
$MgEr_xFe_{2-x}O_4$
x=0.00
Crystallization
Melting or Fusion Point
Heat flow (mW)
Temperature (°C)
4.84
4.82
4.80
4.78
4.76
4.74
204
205
206
207

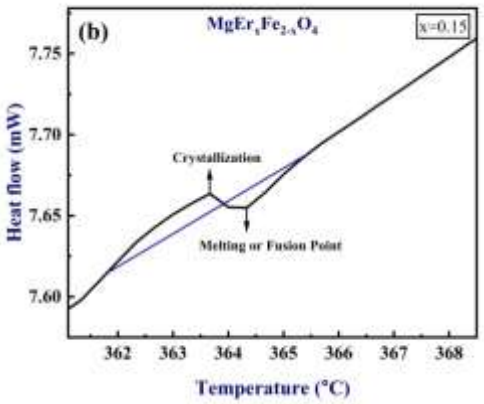
(b)
$MgEr_xFe_{2-x}O_4$
x=0.15
Crystallization
Melting or Fusion Point
Heat flow (mW)
Temperature (°C)
7.75
7.70
7.65
7.60
362
363
364
365
366
367
368

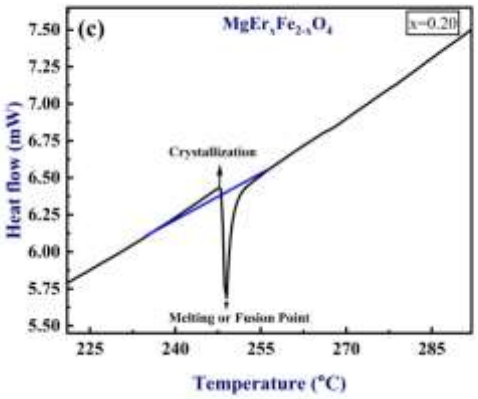
(c)
$MgEr_xFe_{2-x}O_4$
x=0.20
Crystallization
Melting or Fusion Point
Heat flow (mW)
Temperature (°C)
7.50
7.25
7.00
6.75
6.50
6.25
6.00
5.75
5.50
225
240
255
270
285

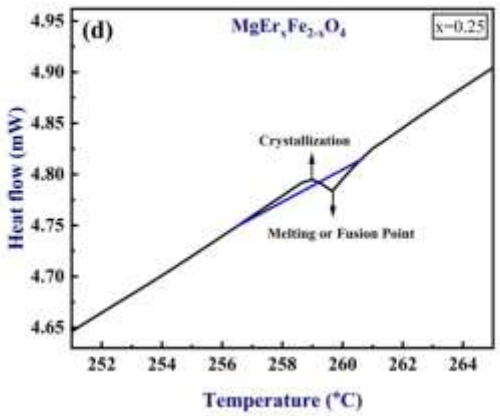
(d)
$MgEr_xFe_{2-x}O_4$
x=0.25
Crystallization
Melting or Fusion Point
Heat flow (mW)
Temperature (°C)
4.95
4.90
4.85
4.80
4.75
4.70
4.65
252
254
256
258
260
262
264

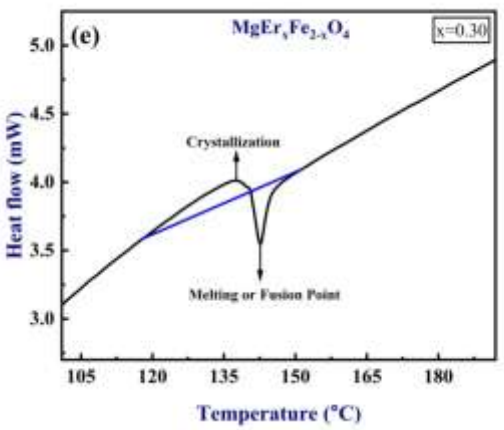
(e)
$MgEr_xFe_{2-x}O_4$
x=0.30
Crystallization
Melting or Fusion Point
Heat flow (mW)
Temperature (°C)
5.0
4.5
4.0
3.5
3.0
105
120
135
150
165
180

Fig 9. Heat flow plots from DSC for $MgEr_xFe_{2-x}O_4$ (a) x=0.00 (b) x=0.15 (c) x=0.20 (d) x=0.25 and (e) x=0.30 samples

The corresponding melting transitions for the Er-doped compositions take place at 361.01 °C (7.59 mW), 248.98 °C (5.69 mW), 259.67 °C (4.78 mW), and 142.77 °C (3.54 mW), respectively, while the crystallization temperatures change to 363.68 °C (7.66 mW), 247.76 °C (6.43 mW), 258.94 °C (4.79 mW), and 137.37 °C (4.01 mW). The higher thermal stability resulting from Er^{3+} incorporation into octahedral sites, which fortifies local bonding heterogeneity and raises the energy barrier for atomic rearrangement, is reflected in the first increase in crystallization temperature and heat flow at moderate Er concentrations [13]. XRD confirms that the decrease in crystallization and melting temperatures with increasing Er concentration is due to enhanced lattice distortion, micro-strain, and smaller crystallites, all of which together enable an earlier beginning of structural relaxation and phase change [14, 15].

The retention of a single-phase cubic spinel structure across the studied temperature range is confirmed by the broad breadth of the DSC characteristics and the lack of sharp endothermic or exothermic peaks, which point to progressive crystallization and melting processes rather than abrupt phase transitions. Since lattice strain and defect states brought on by Er substitution both affect thermal activation processes and electronic structure at the same time, these thermal trends are in line with the observed optical band-gap narrowing. Overall, the DSC results show that Er^{3+} substitution successfully modifies the temperature sensitivity of magnesium ferrites while maintaining structural integrity, emphasizing their appropriateness for multifunctional, thermally stable applications.

3.10 Differential thermal analysis (DTA) and thermogravimetric analysis (TGA)

Using simultaneous TGA-DTA analysis, the thermal stability and breakdown behavior of $MgEr_xFe_{2-x}O_4$(x=0.00, 0.15, 0.20, 0.25, and 0.30) nano-ferrites were examined in the temperature range of ambient temperature to 1000 °C, as illustrated in Fig. 10 (a-e). As is typical of spinel ferrites produced chemically, all compositions show a multistep weight-loss behavior along with broad endothermic and exothermic features in the DTA curves [13]. The removal of physically adsorbed moisture and remaining volatile species from the sample surface is responsible for the initial weight loss that was noted below ~200 °C (≈0.35-1.16%). As frequently documented for ferrite systems, a second weight-loss stage that occurs between ~200 and 450 °C (≈0.52-3.78%) relates to the breakdown of leftover organic materials and the removal of hydroxyl groups associated with precursor residues [15]. Densification, structural rearrangement, and the progressive creation of the thermodynamically stable spinel phase are linked to the slow mass loss that lasts up to about 700 °C [14]. The weight loss for all compositions becomes insignificant beyond about 700 °C, showing the high thermal stability of the $MgEr_xFe_{2-x}O_4$ ferrites and signaling the completion of phase formation.

The thermal response is greatly affected by the addition of Er^{3+} ions. Er-substituted samples show a somewhat higher total weight loss at intermediate temperatures compared to undoped $MgFe_2O_4$. This can be explained by greater lattice distortion and defect density caused by the

larger ionic radius of Er^{3+} at octahedral sites [13, 15]. Nevertheless, the Er-doped samples show better thermal stability at higher temperatures, as seen by the mass stabilizing above around 700 °C and the lack of sharp breakdown stages. This behavior is in line with DSC findings showing expanded crystallization and melting characteristics, as well as XRD results confirming the creation of a single-phase cubic spinel structure. While the lack of abrupt thermal events points to gradual ordering rather than first-order phase transitions, the broad DTA peaks seen in the 300-600 °C range are linked to crystallization and cation redistribution processes inside the spinel lattice [14, 15]. Together, these findings show that Er^{3+} substitution increases

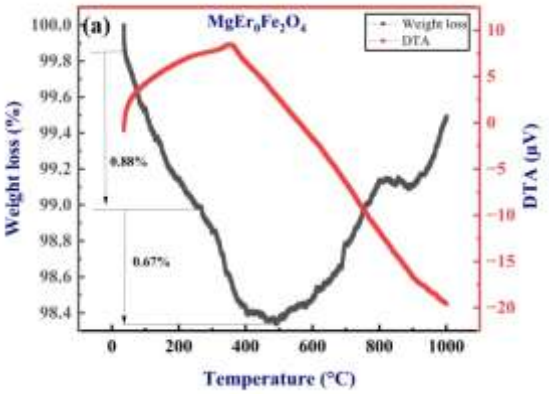

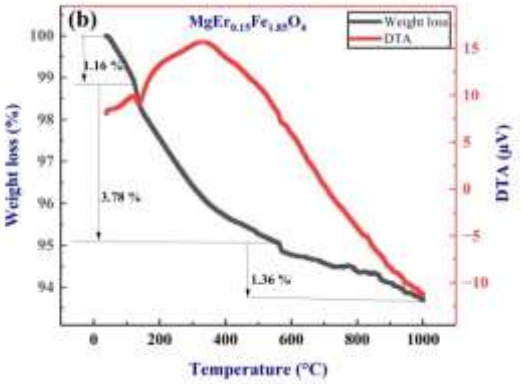

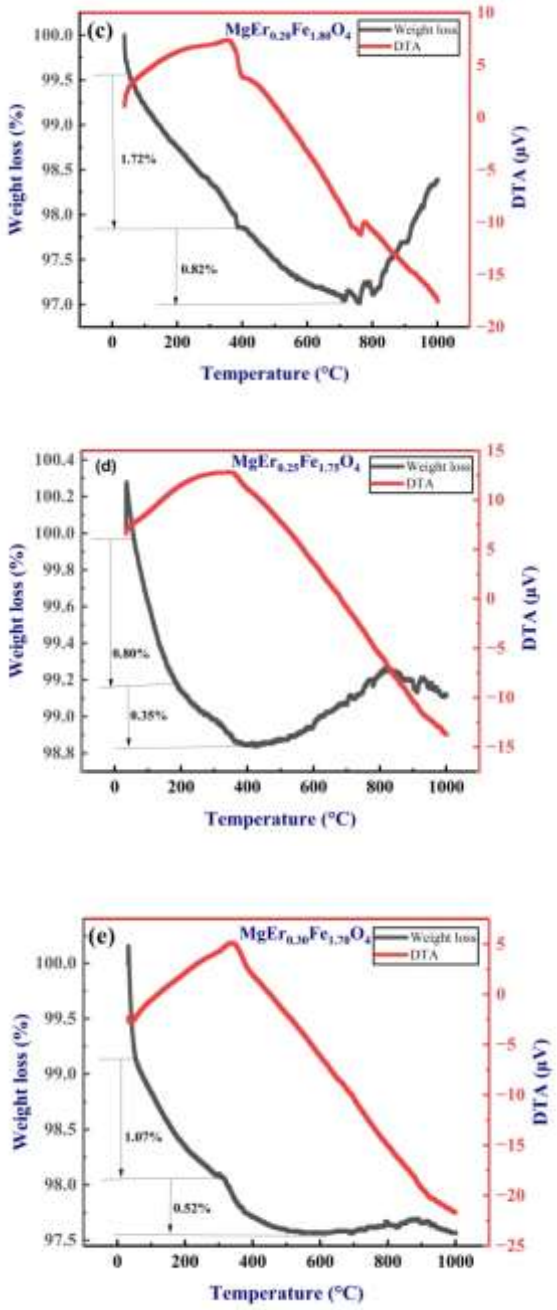

Fig 10. TGA-DTA plots of $MgEr_xFe_{2-x}O_4$ (a) x=0.00 (b) x=0.15 (c) x=0.20 (d) x=0.25 and (e) x=0.30 samples.

lattice disorder at lower temperatures while maintaining structural integrity and thermal robustness at higher temperatures, making $MgEr_xFe_{2-x}O_4$ appropriate for high-temperature magnetic and optoelectronic applications.

4. Conclusions

Rietveld-refined XRD patterns show that all $MgEr_xFe_{2-x}O_4$(x = 0.00, 0.15, 0.20, 0.25, and 0.30) nano-ferrites samples crystallize in a single-phase cubic spinel structure (Fd - 3m). The UV-Vis absorption spectra of $MgEr_xFe_{2-x}O_4$ nanoparticles display a sizable absorption band in the 600-650 nm region. The observed and calculated profiles showed excellent agreement with no secondary phases. Er^{3+} replacement changes the absorbance intensity due to differences in cation distribution and lattice deformation. These results demonstrate that both Er doping and thermal treatment effectively adjust the optical properties of $MgEr_xFe_{2-x}O_4$ ferrites. Er doping successfully tunes the optical band gap of $MgEr_xFe_{2-x}O_4$ ferrites, making them appealing choices for photocatalytic, sensor, and visible-light-driven optoelectronic applications. Strong thermal stability of the spinel phase is demonstrated by the DSC curves of $MgEr_xFe_{2-x}O_4$, which show a broad endothermic zone with no abrupt transitions up to 400 °C and an endothermic peak below ~100 °C as a result of moisture elimination. Er substitution marginally modifies the heat-flow behavior, suggesting improved lattice stabilization without phase change. Er substitution slightly modifies the crystallization slope, suggesting enhanced thermal stabilization and defect-controlled grain growth without phase transition. The TGA-DTA curves reveal a considerable dopant-dependent change in thermal transitions, exhibiting the highest crystallization and melting temperatures, indicating increased thermal stability.

References:

[1]. A. Goldman, Modern Ferrite Technology, 2nd ed., Springer, New York, 2006. DOI: https://doi.org/10.1007/978-0-387-29413-1
[2]. Valenzuela R. Magnetic Ceramics. Cambridge University Press; 1994.
[3]. Ranga R, Kumar K, Kumar A. (2023)Influence of Ce^{3+} ion doping on structural, morphological, magnetic, dielectric and optical properties of $Mg_{0.5}Ni_{0.5}Fe_{2-x}Ce_xO_4$ ($0 \leq x \leq 0.1$) ferrite nanoparticles synthesized via coprecipitation method, Journal of Magnetism and Magnetic Materials. 588, 171496.DOI: https://doi.org/10.1016/j.jmmm.2023.171496
[4]. Pandey B, Srivastava RC, Joshi CS, Verma HK (2025). Effect of cerium ion doping: Alteration in structural, dielectric and magnetic properties of manganese ferrite nanoparticles. Physica B: Condensed Matter. 711, 417302.DOI: https://doi.org/10.1016/j.physb.2025.417302.
[5] Dojčinović MP, Vasiljević ZZ, Pavlović VP, et al. (2021) Structural and magnetic correlations in Mg-based spinel ferrites. Journal of Alloys and Compounds 855, 157429. DOI: https://doi.org/10.1016/j.jallcom.2020.157429
[6] Tangcharoen T. (2024) Structural stability and magnetic properties of $MgFe_2O_4$ spinel ferrite prepared at different calcination temperatures. Results in Materials 23, 100596. DOI: https://doi.org/10.1016/j.rinma.2024.100596

[7] Islam S, Rahman ML, Moni MR, et al. (2023) Structural, optical and thermal properties of spinel ferrite nanoparticles synthesized via sol–gel route. Arabian Journal of Chemistry 16, 105186.DOI: https://doi.org/10.1016/j.arabjc.2023.105186
[8] Basfer NM, Al-Harbi N. (2023) Rare-earth-doped spinel ferrites: structural, optical and photocatalytic properties. Journal of King Saud University – Science 35, 102436. DOI: https://doi.org/10.1016/j.jksus.2023.102436
[9] Gabal MA, Al-Angari YM. (2020) Magnetic and electrical properties of rare-earth substituted magnesium ferrites. Ceramics International 46, 20110–20118. DOI: https://doi.org/10.1016/j.ceramint.2020.05.234
[10] Slimani Y, Almessiere MA, Güngüneş H, et al. (2022) Rare-earth doped spinel ferrites for multifunctional applications. Journal of Materials Research and Technology 18, 2030–2042.
DOI: https://doi.org/10.1016/j.jmrt.2022.03.020
[11]. A. T. Raghavender, D. Pajic, K. Zadro, T. Milekovic, P. V. Rao, K.M. Jadhav, D. Ravinder, (2007) Synthesis and magnetic properties of $NiFe_{2-x}Al_xO_4$ nanoparticles, Journal of Magnetism and Magnetic Materials 316 (1), 1-7.DOI: https://doi.org/10.1016/j.jmmm.2007.03.204
[12]. J. Adam, K. Vijaya Kumar, N. Hari Kumar, (2024), Er3+ ion-doped Mg-Zn nanoferrite: Properties and applications in dielectric, magnetic, structural, and optical domains affected by calcination temperature, Inorganic Chemistry Communications 167, 112698. DOI: https://doi.org/10.1016/j.inoche.2024.112698
[13] S. Tholkappiyan, A. Vishista, (2015)Combustion synthesis of $MgFe_{2-x}Er_xO_4$ nanoparticles: Structural, optical and magnetic properties, Materials Science in Semiconductor Processing, 40, 631–642.DOI: https://doi.org/10.1016/j.mssp.2015.06.076
[14] S.J. Salih, W. M. Mahmood (2023), A comprehensive review on magnetic spinel ferrite (MFe_2O_4) nanoparticles: structural and functional properties, Heliyon, 9 (2023) e17364. DOI: https://doi.org/10.1016/j.heliyon.2023.e16601
[15] Shashi Kumar Jakkaraju, Katrapally Vijaya Kumar, N. Hari Kumar, (2025) Influence of calcination temperature on gadolinium doped magnesium-zinc ferrite nanoparticles: Structural, optical, and photocatalytic properties for water splitting applications, Next Materials 8, 100705. DOI: https://doi.org/10.1016/j.nxmate.2025.100705
[16] M. Iqbal et al., (2020)Rare-earth doped spinel ferrites: Correlation between structure and optical properties, Journal of Magnetism and Magnetic Materials, 512, 166991. DOI: https://doi.org/10.1016/j.jmmm.2020.166991
[17] B.R. Judd, (1962) Optical absorption intensities of rare-earth ions, Physical Review, 127, 750–761.DOI: https://doi.org/10.1103/PhysRev.127.750
[18] Slimani, Y., Almessiere, M.A., Baykal, A., et al., (2020) "Optical and magnetic properties of rare-earth substituted spinel ferrites," Ceramics International 46, 19194-19204. DOI: https://doi.org/10.1016/j.ceramint.2020.04.285
[19] Kambale, R.C., Shaikh, P.A., Kolekar, Y.D., (2019) "Effect of rare-earth substitution on structural and optical properties of spinel ferrites," Journal of Alloys and Compounds 774, 1002–1011.DOI: https://doi.org/10.1016/j.jallcom.2018.10.038

[20] Almessiere, M.A., Slimani, Y., Baykal, A., (2021) "Influence of rare-earth ions on electronic structure and optical response of ferrites," Materials Science in Semiconductor Processing 121, 105325.DOI: https://doi.org/10.1016/j.mssp.2020.105325
[21] Prasad, S., Dolia, S.N., Pareek, S.P., (2018) "Band gap tuning and optical absorption in rare-earth doped ferrite nanoparticles," Optik 172, 864–872.
DOI: https://doi.org/10.1016/j.ijleo.2018.07.098
[22] Manikandan, A., Kennedy, L.J., Vijaya, J.J., (2020) "Rare-earth-doped spinel ferrites for optical and photocatalytic applications," Journal of Materials Science: Materials in Electronics 31, 20498–20510.DOI: https://doi.org/10.1007/s10854-020-04563-1
[23] Rahman, M.M., Hossain, M.S., Islam, M.A., (2022) "Defect-mediated optical absorption in nanocrystalline ferrites," Materials Chemistry and Physics 288, 126364.
DOI: https://doi.org/10.1016/j.matchemphys.2022.126364
[24] Aparna Nadumane, Krushitha Shetty, K.S. Anantharaju, H.P. Nagaswarupa, Dinesh Rangappa, Y.S. Vidya, H. Nagabhushana, S.C. Prashantha, (2019) Sunlight photocatalytic performance of Mg-doped nickel ferrite synthesized by a green sol- gel route, J. Sci.: Adv. Mater. Devices 4, 89–100. DOI: https://doi.org/ 10.1016/j.jsamd.2018.12.002.
[25] H.D.ChoG.Mohan Kumar, D.J. Lee, J. Kumar, C. Siva, P. Ilanchezhiyan, D.Y. Kim, T.W. Kang, (2021) Elevating the charge separation of MgFe2O4 nanostructures by Zn ions for enhanced photocatalytic and photoelectrochemical water splitting, Chemosphere 283, 131134, DOI: https://doi.org/10.1016/j. chemosphere.2021.131134.
[26] Bindhyabasinee Mishra, Bhagyashree Munisha, Jyotirmayee Nanda, Shradha Suman, (2022) Hydrothermally synthesized magnesium doped zinc ferrite nanoparticles: an extensive study on structural, optical, magnetic, and dielectric properties, Mater. Chem. Phys. 292, 126791, DOI: https://doi.org/10.1016/j. matchemphys.2022.126791.
[27] Dong Suk Kim, Seung-Yeop Kwak, (20070 The hydrothermal synthesis of mesoporous TiO2 with high crystallinity, thermal stability, large surface area, and enhanced photocatalytic activity, Appl. Catal. A: Gen. 323, 110–118, DOI: https://doi.org/ 10.1016/j.apcata.2007.02.010.
[28] T. Itoi, T. Inazawa, M. Yamasaki, Y. Kawamura, M. Hirohashi, (2023) Microstructure and mechanical properties of Mg Zn Y alloy sheet prepared by hot-rolling, Mater. Sci. Eng. A. 560, 216–223, DOI: https://doi.org/10.1016/j.msea.2012.09.059.
[29] X. Li, L. Zhao, J. Yu, et al., (2020) Water splitting: from electrode to green energy system, Nano-Micro Lett. 12, 131, DOI: https://doi.org/10.1007/s40820-020-00469-3.
[30] D.M. Tejashwini, H.V. Harini a, H.P. Nagaswarupa, Ramachandra Naik, Sujatha Harlapur, N. Basavaraju, (2024) Nanoferrites in photocatalytic wastewater treatment: advancements, characterization, and environmental implications, Results Chemi 7, 101247, DOI: https://doi.org/10.1016/j.rechem.2023.101247.